

Received: 02 April, 2025

Accepted: 10 April, 2025

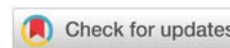
Published: 11 April, 2025

\*Corresponding author: Delia Teresa Sponza, Environmental Engineering Department, Engineering Faculty, Dokuz Eylül University, Buca İzmir, Turkey, E-mail: [delya.sponza@deu.edu.tr](mailto:delya.sponza@deu.edu.tr)

**Keywords:** Energy; Retainment; Crystalline elastomer; Lead zirconate titanate

**Copyright License:** © 2025 Sponza DT. This is an open-access article distributed under the terms of the Creative Commons Attribution License, which permits unrestricted use, distribution, and reproduction in any medium, provided the original author and source are credited.

<https://www.agriscigroup.us>



## Research Article

# Energy Retainment from Crystalline Elastomer (CrEI) and Lead Zirconate Titanate (PbZrT)

Delia Teresa Sponza\*

Environmental Engineering Department, Engineering Faculty, Dokuz Eylül University, Buca İzmir, Turkey

ORCID: Sponza DT: <https://orcid.org/0000-0002-4013-6186>

## Abstract

Pyroelectric materials that can generate electric charges when subjected to temperature changes dependent on renewable energy. Conventional pyroelectric energy harvesters suffer from low output. In this study, a nanocomposite was generated with crystalline elastomer (CrEI) and pyroelectric lead zirconate titanate (PbZrT) nanoparticles. As a result, a heat harvesting device with high output was generated. The overall pyroelectricity is enhanced by the secondary pyroelectricity generated from the thermal stress imposed on the CrEI. The monodomain CrEI/ PbZrT NCs with enhanced energy production. The monodomain CrEI/ PbZrT NCs film with a PbZrT ratio of 3.2 wt % exhibited a current of 2.99 nA and a voltage of 6.99 V. This energy harvester can charge capacitors and power electronic devices.

## Introduction

In a world, more than 70% of the total energy generated is dissipated as wasted heat [1]. Harnessing the wasted heat not only provides a carbon reduction but also generates sustainable energy. The direct method of converting heat to electricity depends on the Seebeck effect, which uses the temperature gradient across a thermoelectric device to manage charge carriers from the hot side to the cold side [2]. However, in an outdoor environment, the temperature distribution is not homogenous, therefore, with the conventional Seebeck effect is not important to harvest energy, or less energy is retained. The pyroelectric effect increases when pyroelectric materials exhibit a change in the polarization with temperature. It can be defined by the pyroelectric coefficient [3,4], which contains two stages. The first is the primary pyroelectric effect, defined as a variation in temperature ending with a change in electric displacement. The second is the secondary pyroelectric effect, which can be defined by temperature variations and causes stress in the material by thermal expansion. Then this stress induces additional electric variations via a piezoelectric process [5]. The secondary pyroelectric effect is a piezoelectric effect detected without stress stimulation, only through temperature variation [6].

Pyroelectric nanoproducers have been generated to harvest waste heat based on different pyroelectric materials such as zinc oxide [7], barium titanate [8], lead zirconate titanate [9], potassium niobate (KNbO<sub>3</sub>) [10], polyvinylidene fluoride (PVDF) [11–13]. When ceramic materials provide a high magnitude of pyroelectric coefficient, their high rigidity greatly limits their applications as wearable electronics and smart sensors. Polymers such as PVDF are commonly used in flexible pyroelectrics. However, their pyroelectric performance is limited for PVDF [10,13]. Therefore, a hybrid generator was developed by combining pyroelectric and piezoelectric effects to harness both properties from a single nanogenerator. This was achieved by applying heat, as all pyroelectric materials inherently exhibit piezoelectric properties [14,15]. However, the pyroelectric signal itself is not enhanced in these material systems. The enhancement comes from responses from other types of stimulation. That is, two or more different stimuli need to be applied simultaneously. To enhance the overall pyroelectricity of the pyroelectric effect heat should be changed. The secondary pyroelectric coefficient is an intrinsic property of the pyroelectric materials. It was mentioned that the thermal expansion due to phase change can elevate the pyroelectric energy conversion density. It was shown that the pyroelectricity coefficient of the ferroelectric BaTiO<sub>3</sub> can be increased 4.8 times when operating near its Curie temperature of 140 °C

since the stress affects the heat variation. However, operating near the Curie temperature provides faster depolarization of the ferroelectric materials when the pyroelectric devices fail. Liquid crystalline elastomers (*CrEI*) with the intrinsic molecular anisotropy of the liquid crystal can generate stress and undergo shape transformations during heating above the isotropic phase transition temperature,  $T_{NI}$  [16–18]. Below  $T_{NI}$ , LC molecules can be aligned all in one direction by producing monodomain. When LC molecules are aligned only in a small domain, polydomains are formed. Upon heating above  $T_{NI}$ , LC molecules lose their orientations. For monodomain LCEs, the sample shrinks exerting large stress. For polydomain *CrEI*s, the stress generated in individual domains was deleted in the samples. In addition, functional nanoparticles *CrEI* nanocomposites [18] can be made to be responsive to light [20], electric field [21], and magnetic field. However, fewer studies were detected in their applications in energy harvesting [22–25]. Given the large thermal stress of *CrEIs*, they are important candidates for integration with pyroelectric materials. As a result, the thermally induced stress in *CrEIs* could be transferred to pyroelectric materials. This causes the production of a secondary pyroelectric effect improving the original pyroelectric signal. A layer was applied of *CrEI* on the poly (dimethylsiloxane side of the PVDF/PDMS) triboelectric device, to bend the *CrEI* layer during heating by producing a triboelectric and secondary pyroelectric signals. It generated a PVDF/*CrEI* film to facilitate the simultaneous capture of primary and secondary pyroelectric signals. However, their performance remains low with the maximum output voltage since the stress generated in the *CrEI* layer cannot be effectively transferred to PVDF [26].

In this study a *CrEI* NC doped with *PbZrT* NPs to generate an output current of 3.22 nA and a voltage of 6.99 V, corresponding to  $p = -3.96 \text{ nC cm}^{-2} \text{ K}^{-1}$ . Since the monodomain versus polydomain and boundary conditions of the *CrEI* NC film can affect the effective interactions between the *CrEI* NC and *PbZrT* NPs. It was studied their effect on the output performance during assays. The *CrEI* / *PbZrT* NCs can power light-emitting diodes with multiple cycles, demonstrating the potential applications of flexible energy harvesters for self-powered devices.

## Materials and methods

### Materials

*PbZrT* and  $\text{BaTiO}_3$  were purchased from Sigma Aldrich. TMSPMA ( $\geq 97\%$ ), DPA (99%), EDDT (95%), PETMP ( $>95\%$ ), PEGDA and 1, 1'-azobis(cyclohexanecarbonitrile) (98%) were purchased from Sigma-Aldrich. Ethanol (99.5%), hydrochloric acid (HCl, 50%), and acetic acid were purchased from Merck. The *CrEI* ( $>95\%$ ) was purchased from Merck Technologies Inc. The deionized water was produced by a Milli-Q Ultra Pure system and it was used in all experiments.

### Generation of *PbZrT* NCs

*PbZrT* NPs were ball milled to an average size of  $<1.1 \mu\text{m}$ . Then, 3.92 g of *PbZrT* NCs was dissolved in a 300-ml ethanol

solution with 6 ml of TMSPMA and a 145- $\mu\text{l}$  acetic acid aqueous solution (acetic acid to water ratio was 1:8). The mixture was sonicated for 40 hours. The final product was washed with ethanol to remove any unreacted TMSPMA. Then the mixture was centrifuged at 3500 rpm for 25 min. After the ethanol solution was settled, the *PbZrT* NCs were collected and dried at 70 °C overnight.

### Generation of *CrEI/PbZrT* NCs

8 g of RM was dissolved in 1.67 g of toluene by heating the mixture in a 100 °C oven for 25 min. The saturated solution was cooled at room temperature. Then, 0.288 g of tetra-thiol cross-linker PETMP, 1.298 g of dithiol chain extender EDDT, 0.19 g of thermal initiator 1,1'-azobis(cyclohexanecarbonitrile), and a desired amount of TMSPMA-modified *PbZrT* NCs (1.5, 2.0, 4.0, AND 6.0 g) were added. The mixture was maintained at 70 °C oven for 25 min to complete the mixing. The catalyst DPA with a ratio of 0.90 g to 4 wt % toluene was put into the mixture and stirred after cooling to 20 °C temperature. The mixture was vacuumed for 2 min. Then, the viscous solution was poured into a mold using 1.3-mm-thick VHB tape (4M) as the spacer and maintained for 20 hours to finish the thiol-arylate Michael addition reactions. The produced *CrEI/PbZrT* NCs were placed into a 70 °C oven for 24 hours to remove the solvent. The polydomain sample was obtained by directly cross-linking the *CrEI/PbZrT* NCs mixture in a 100 °C oven for 24 hours [27]. For the monodomain sample, the *CrEI/PbZrT* NCs film was stretched at a 100% strain, and fixed on a glass slide in a 100 °C oven for 24 hours [28]. For generation of *CrEI/PbZrT* NCs 6.25 g of *CrEI* and 3.2 g of *PbZrT* were used. The generated samples were poled under 1.2 kV  $\text{mm}^{-1}$  at 115 °C for 6 hours between two indium tin oxide glasses. After poling, the *CrEI/PbZrT* NCs were assembled using copper tapes as electrodes and encapsulated with Kapton tapes.

### Physicochemical properties of *CrEI/PbZrT* NCs

SEM was used to characterize the size and size distribution of *PbZrT* NPs, and the dispersity of the *PbZrT* in *CrEI* NPs. FTIR spectroscopy was performed on KBr pellets. For the measurement of the pyroelectric performance, a high-power light bulb was used to change the temperature of the film, and the distance between the film and the light bulb was maintained at 25 cm to obtain a constant heating rate. The temperature was monitored by a thermal imager. The open-circuit voltage and the short-circuit current were measured by a DMM6500. Differential scanning calorimetry tests were performed on the TA Instruments. The *CrEI/PbZrT* NC film with 30.1 wt % *PbZrT* was cut into small pieces. Samples were heated and cooled at a ramping rate of 15 °C/min under  $\text{N}_2$  for two cycles, from -60 °C to 160 °C. The chemical composition of *PbZrT* NC was measured by an electron microscope with an energy dispersive X-ray spectrometer (Horiba, Japan).

## Results

### Generation of *CrEI/PbZrT* NCs

In the *CrEI/PbZrT* NC, *PbZrT* NPs generate the primary

pyroelectricity, while the thermal stress is generated from the *CrEI* and emitted to *PbZrT* NPs to enhance the secondary pyroelectricity. The *CrEI* film is prepared by the two-step thiol-acrylate Michael addition reactions [29]. First, the *CrEI* monomer 1,4-bis-[4-(3-acryloyloxypropoxy)benzoyloxy]-2-methylbenzene (RM), the chain extender 2,2'-(ethylenedioxy) diethanethiol (EDDT), and the cross-linker pentaerythritol tetrakis(3-mercaptopropionate) (PETMP) are mixed together with *PbZrT* NPs to enhance the surface methacrylate groups. A 0.9:0.3:0.9 molar ratio of acrylates to thiols and a 12:0.9 molar ratio of EDDT to PETMP are added to enhance the flexibility. Then, dipropylamine (DPA), is added to the mixture, at 90 °C to prepare the polydomain samples. The monodomain samples are prepared by stretching the as-cast films to 100% strain before thermal curing. The monodomain alignment of the *CrEI* films is verified by the polarized optical microscope equipped with cross-polarizers. After mixing with, *PbZrT* NPs, they can show reversible elongation upon heating and cooling processes.

The polydomain and monodomain *CrEI/PbZrT NC* containing 30.1 wt % *PbZrT* are 1.0 and 1.7 MPa in the longitudinal direction, respectively. It is much smaller than that of PVDF, 1.6 to 2.8 GPa [30–32]. In most *CrEI* composites for actuation applications, nanofiller loadings are typically less than 4 wt %, above which the viscosity of the mixture is increased substantially, and thus, the nanofillers cannot disperse uniformly [33–35]. To address this issue, we surface modify *PbZrT* NPs with 3-(trimethoxysilyl)propyl methacrylate (TMSPMA), which can covalently cross-link with the *CrEI* matrix via the thiol groups [36]. As a result, a very high loading (10 to 60 wt %) of *PbZrT* NPs can be introduced in our *CrEI* matrix, which is important to generate larger electric signals.

### FTIR analysis results of *PbZrT* NPs

The Fourier transform infrared (FTIR) spectrum of the pristine *PbZrT* NPs exhibited disturbances for carbonyl and alkene groups at 1719 and 1642  $\text{cm}^{-1}$ , respectively (Figure 1). The modified *PbZrT* NPs clearly showed excellent surface functionalization (Figure 1).

### Scanning Electron Microscopy (SEM) images of *PbZrT* and *CrEI/PbZrT NCs*

The scanning electron microscopy (SEM) images of *PbZrT*

NPs and *CrEI/PbZrT* Nanocomposites were illustrated in Figures 2a–2c. The mean diameter of the *PbZrT* NPs was approximately 258 nm and are randomly distributed in the *CrEI* matrix without exhibited an aggregation. At high loading, the covalent bonding between *PbZrT* NPs and the *CrEI* matrix improved the interfacial contact by facilitating the efficient transfer of thermal stress from *CrEI* to *PbZrT* NPs [37]. This is very important to built up a substantial secondary pyroelectric effect. It was used a thermal curing to provide an uniform cross-link in a thick film with a diameter of 1.2 mm.

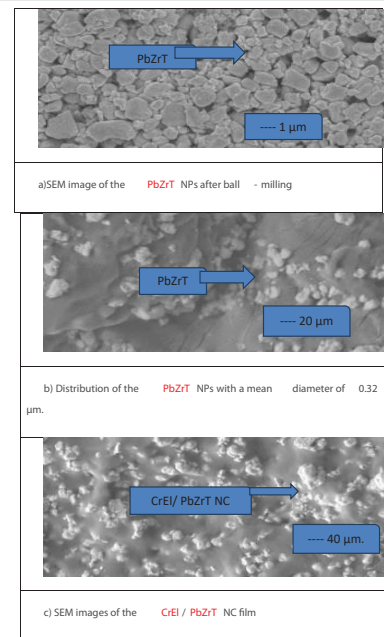


Figure 2: SEM images of *PbZrT* (a,b) and *CrEI/PbZrT NC* (c).

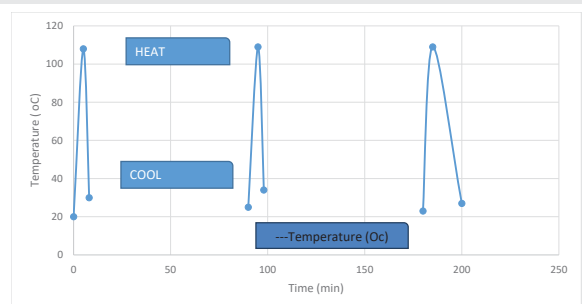


Figure 2a: Effect of temperature increasing on *CrEI/PbZrT NCs* after heating and cooling processes

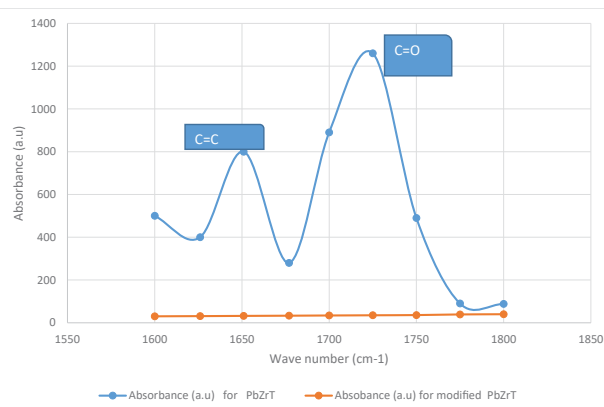


Figure 1: FTIR analysis results of *PbZrT NCs*.

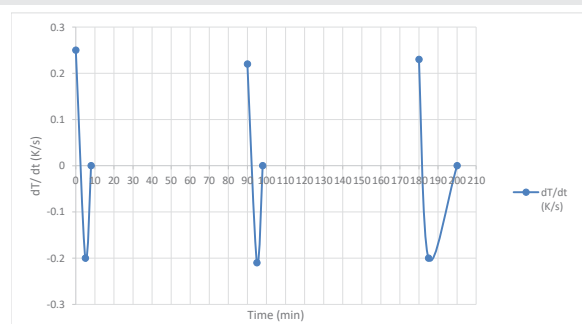


Figure 2b: Effect of the cooling process on *CrEI/PbZrT NCs*.

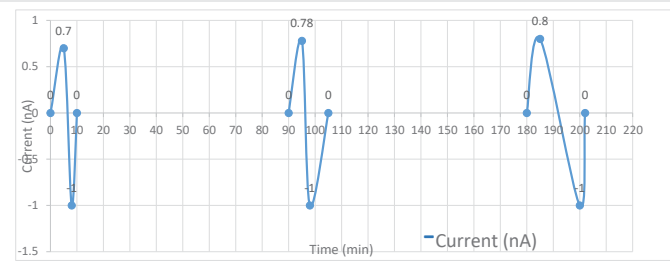


Figure 2c: Cyclic current variations.

The cross-linked *CrEl/PbZrT NCs* as films are placed between two copper films as the top and bottom electrodes (Figure 1c) for poling at an electric field of  $1.4 \text{ kV mm}^{-1}$  for 6 hours, aligning the dipole moments of *bZrT NPs* across the sample thickness. When the temperature changes, the primary pyroelectric effect of *PbZrT*, is doped with the secondary pyroelectric effect from the thermally induced stress in *CrEl*. This phenomenon is expected to provide power to an external circuit. In this way, the energy from temperature fluctuations in the surroundings can be harvested.

### Energy-Dispersive Spectroscopy (EDS) analysis of *PbZrT NC*

EDS analysis was done to obtain chemical compositions of the *PbZrT NC*. Table 1 confirmed that *PbZrT NC* contains lead (Pb), zirconium (Zr), titanium (Ti), oxygen (O), and tin (Sn).

### Pyroelectric harvesting from *CrEl/PbZrT NCs*

To detect the output current, the *CrEl/PbZrT NCs* is irradiated by a torch lamp every 8 min to heat and ten to cool for 100 min at temperatures between  $20 \text{ }^\circ\text{C}$  and  $70 \text{ }^\circ\text{C}$  (Figure 2a).

The cooling duration is long for the temperature to return to  $20 \text{ }^\circ\text{C}$  after one cycle (Figure 2b).

It is noted that the peak temperature of  $58 \text{ }^\circ\text{C}$  is above the  $T_{NI}$  ( $52.5 \text{ }^\circ\text{C}$ ) of the *CrEl/PbZrT NCs* LCE/PZT composite For pyroelectricity, the output current with Eq. (1).

$$I = pA \frac{dT}{dt} \tag{1}$$

where  $A$  is the effective area of the pyroelectric device, and  $dT/dt$  is the rate of temperature change. Since  $p$  and  $A$  are fixed for a certain system, the output current should have a similar profile as  $dT/dt$ , which is calculated with a maximum heating rate of  $0.25 \text{ K s}^{-1}$  (Figure 2c) at *CrEl/PbZrT NCs* containing  $30.3 \text{ wt } \% \text{ PbZrT NCs}$  (Figure 2c).

In Figure 2c, the peak of the output current of  $0.76 \text{ nA}$  at the maximum heating rate of  $0.20 \text{ K s}^{-1}$ , and the current changes direction when the  $dT/dt$  changes its sign. The voltage profile is also measured with a peak voltage of  $9.8 \text{ mV}$  when the internal impedance of the voltmeter is  $12 \text{ megohms}$  (Figure 2c).

Since the output voltage of the pyroelectric materials is highly dependent on voltmeter parameters, a voltmeter with a larger impedance ( $12 \text{ gigohms}$ ) is used to record the peak voltage of  $6.88 \text{ V}$ . Due to *CrEl/PbZrT NCs* has polarization, we inverse the connection of the upper and bottom surfaces to get the forward and backward current. In this step the electric emission originated from *CrEl/PbZrT NCs* (Figure 2d).

Table 1: Energy dispersive spectrometer (EDS) results of *PbZrT NC*.

Element	Weight (%)
Pb	62
O	21
Ti	6,99
Zr	11,20
Sn	0,34

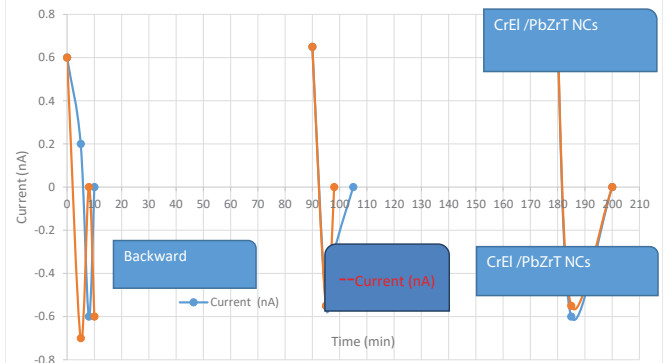


Figure 2d: Cyclic current variations in *CrEl/PbZrT NCs*.

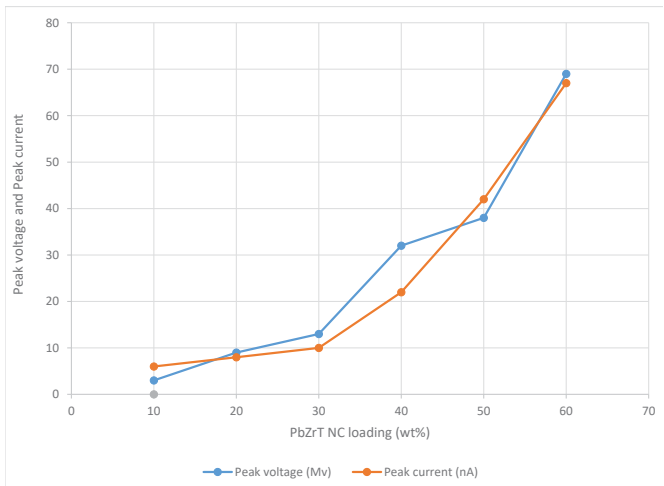


Figure 2e: Peak voltage and peak current of the *CrEl/PbZrT NC* films.

In all samples the *PbZrT NC* loading was  $30.2 \text{ wt } \%$ . As the *PZT* loading is increased from  $18.9$  to  $30.2$ ,  $45.9$ , and  $65.9 \text{ wt } \%$ , respectively, the peak open-circuit voltage increases from  $4.0$  to  $9.3$ ,  $21.3$ , and  $27.4 \text{ mV}$ , respectively. Simultaneously, the short-circuit current increases from  $0.60$  to  $1.92 \text{ nA}$  (Figure 2e).

At the highest loading of  $65.1 \text{ wt } \%$ ,  $p$  is calculated to be  $-3.80 \text{ nC cm}^{-2} \text{ K}^{-1}$ , whose magnitude is  $29\%$  higher than that of the widely used flexible pyroelectric polymer *PVDF* ( $-2.99 \text{ nC cm}^{-2} \text{ K}^{-1}$ ) [13]. Pure *CrEl* shows no noticeable fluctuations in both current and voltage confirming the signals in *CrEl/PbZrT NC* films are generated by the pyroelectric effect instead of thermal stress from *PbZrT* itself.

### Pyroelectric output emissions in on *CrEl* bonding

Since the secondary pyroelectricity here relies on the intimate interactions between *CrEl* and *PbZrT NC* films, the *CrEl*

boundary conditions of the film (fixed or not fixed at ends) can affect the pyroelectric output. When *CrEl* /*PbZrT* NC film, the monodomain samples the disturbances shows a maximum stress of 0.76 MPa, while the polydomain sample shows no apparent stress (Figure 3a).

When *PbZrT* NCs are changed to  $\text{BaTiO}_3$  NPs, the remaining can be dispersed homogeneously in the *CrEl* NPs. The polydomain *CrEl* to  $\text{BaTiO}_3$  ratio was 30.2 wt % with a peak current of 0.65 nA (Figure 3b). It is smaller than that of the polydomain *CrEl* /*PbZrT* NC film with a mass ratio of 37.1 wt %. This is because  $\text{BaTiO}_3$  has a lower magnitude of  $p$  ( $-20.0 \text{ nC cm}^{-2} \text{ K}^{-1}$ ) compared to that of *PbZrT* NCs ( $-26.8 \text{ nC cm}^{-2} \text{ K}^{-1}$ ) [5].

Further increase of the peak current, electrically conducting dopants can be added to reduce the resistance of the composite. For example, 0.27 wt % carbon nanotubes (CNTs) and 0.20 wt % carbon black (CB) are added to the polydomain *CrEl* /*PbZrT* NC with a ratio of 31.1 wt. Under these conditions can be found a peak current of 3.20 nA (Figure 3c). CNTs enhance conductivity, while the addition of CB makes the prepolymer processable instead of doubling CNT loadings as CNTs can substantially increase the viscosity [21].

It is expected that different stresses lead to different secondary pyroelectricity. Even at the same *CrEl* alignment,

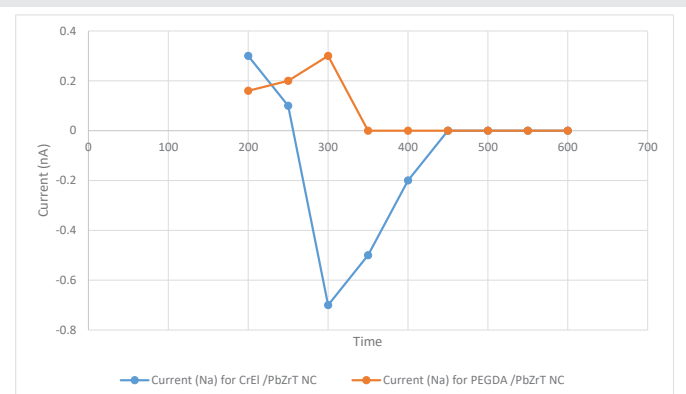


Figure 3a: Comparison of current levels for *CrEl* /*PbZrT* NC film and PEGDA / *PbZrT*.

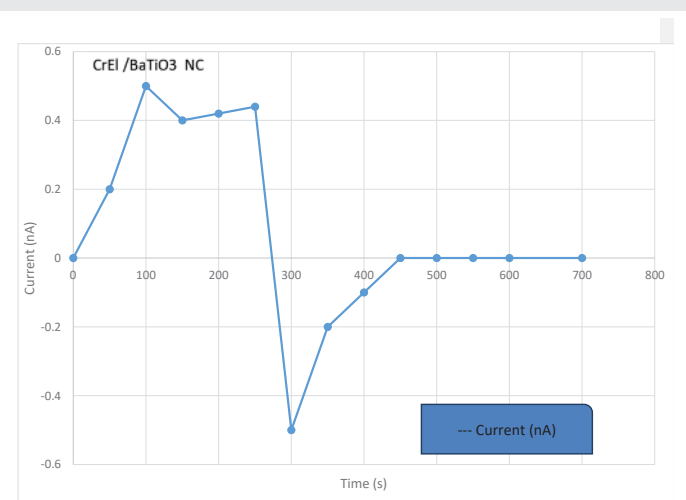


Figure 3b: Current variations in polydomain *CrEl* / $\text{BaTiO}_3$ .

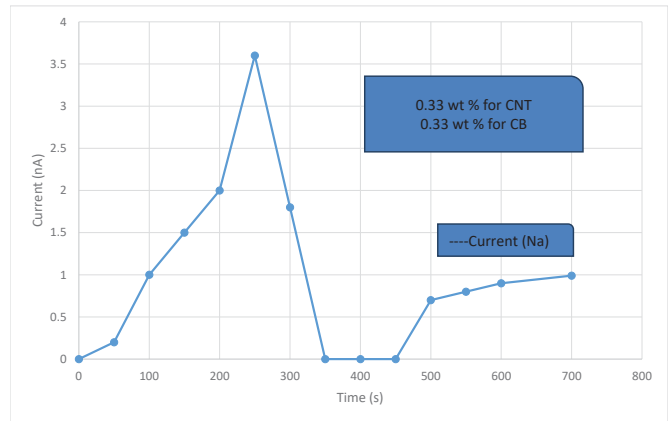


Figure 3c: Variations of current in CNT and CB.

whether the two ends of the film in the longitudinal direction are fixed or not can alter the output current. For the monodomain *CrEl* /*PbZrT* NC, the peak current density is  $0.59 \text{ nA/cm}^2$  with two ends fixed but  $0.33 \text{ nA/cm}^2$  with two ends free (Figure 4a).

In the polydomain *CrEl* /*PbZrT* NC, the peak current density does not vary significantly:  $0.38 \text{ nA/cm}^2$  (fixed) and  $0.35 \text{ nA/cm}^2$  (free) (Figure 4b).

When the *CrEl* /*PbZrT* NC film is heated with a positive value, a negative secondary pyroelectric coefficient will enhance the output current. Now, we conclude that the output current density is higher than the primary contribution,  $0.33 \text{ nA/cm}^2$ . Theoretical calculations give the estimated output current density of  $\sim 0.55 \text{ nA/cm}^2$ , which matches with experimental results of  $0.54 \text{ nA/cm}^2$ .

This approach can be extended to other boundary conditions, for example, a monodomain *CrEl* /*PbZrT* NC film with all ends free. Theoretically, the average stresses from all directions are close to zero, although experimentally, it is difficult to meet this. The output current density should be close to the pure primary contribution,  $0.33 \text{ nA/cm}^2$ , which matches with the experimental result,  $0.32 \text{ nA/cm}^2$ .

Since the secondary pyroelectricity is dependent on intimate interactions between *PbZrT* NCs and *CrEl* NPs, both the disturbances of *CrEl* and the boundary conditions of the *CrEl* /*PbZrT* NC can affect the pyroelectric level. When *CrEl* /*PbZrT* NC is fixed at two ends, the monodomain sample shows a peak stress of 0.57 MPa, while the polydomain sample shows no apparent stress (Figure 4a). It is expected that different stresses lead to different secondary pyroelectricity. Even at the same *CrEl* alignment, whether the two ends of the film in the longitudinal direction are fixed or not can alter the output current. For the monodomain *CrEl* /*PbZrT* NC, the peak current density is  $0.54 \text{ nA/cm}^2$  with two ends fixed but  $0.28 \text{ nA/cm}^2$  with two ends free (Figure. 4b). However, for the polydomain LCE/PZT, the peak current density does not vary much:  $0.35 \text{ nA/cm}^2$  (fixed) and  $0.34 \text{ nA/cm}^2$  (Figure 4c). To investigate the contributions from the primary and secondary pyroelectricity of the LCE/PZT system, we carry out a quantitative analysis as follows.

Changing the boundary conditions alters the stress state

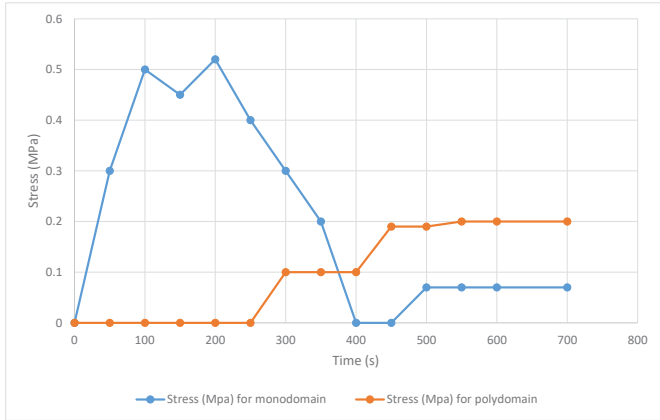


**Figure 4a:** Variation of stress in monodomain and polydomain *CrEI/PbZrT NC*.

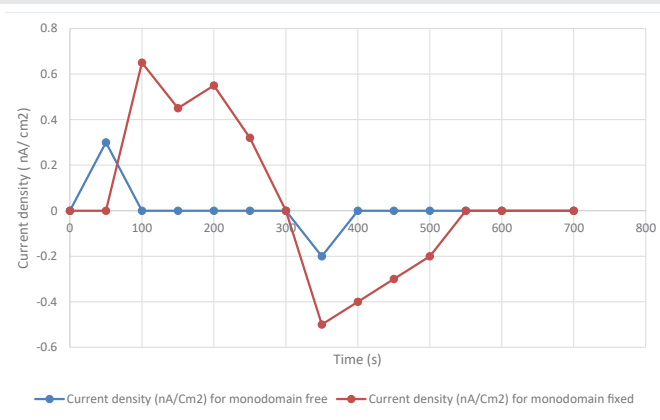


**Figure 4b:** Variation of current density in monodomain-free and fixed *CrEI/PbZrT NC* samples.

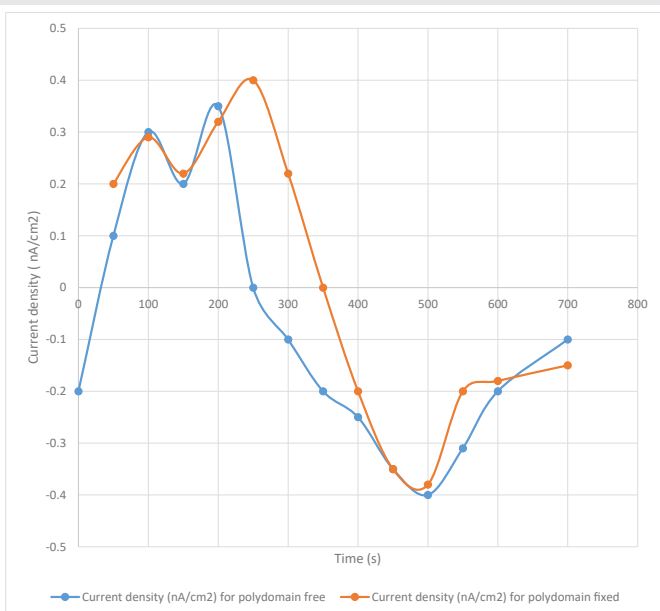


**Figure 4c:** Variation of current density in polydomain free and fixed *CrEI/PbZrT NC* samples.

inside the material and produces different secondary currents  $I_{sec}$ . The stresses and deformations of monodomain *CrEI/PbZrT NC* under the two boundary conditions are shown in Figures 4a,4b as aforementioned above. The greater von Mises stresses

make the secondary effect more prominent in the fixed-end condition than in the free-end condition. More importantly, the primary and secondary effects are synergistic in the fixed-end condition, and their currents are in the same direction, whereas in the free-end condition, the two effects are canceling of each other due to the change in the direction of the stress vector  $S$ . According to the simulation results, the peak total current density generated from the monodomain *CrEI/PbZrT NC* under the fixed-end and free-end conditions are 0.49 nA and 0.33 nA, respectively. Compared with the experimental results, the deviations are 19% and 2%, respectively.

### Finite element method (FEM) simulations

Ferroelectric-type pyroelectric materials demonstrate a primary pyroelectric effect when there is a variation in temperature while the shape and volume remain constant. Nevertheless, this effect is often accompanied by a secondary effect that arises from thermal expansion and piezoelectricity, making it challenging to differentiate them in experiments. To quantify their respective contributions, it is necessary to perform FEM simulations using tools such as a Multmputer physic programme. The Heat Transfer in Solids module simulates the heating and cooling processes of the *CrEI/PbZrT NC* for a specific temperature boundary condition  $T(t)$  (Eq.2).

$$dp Cp \frac{dT}{dt} + d\rho Cu x\Delta T + \Delta X (-dk \Delta T) = 0 \tag{2}$$

The simulations are conducted assuming zero strain in the out-of-plane direction, which is the case of LCE upon heated above TNI. Here,  $dz$  is the width of the samples, is the material density,  $Cp$  is the heat capacity, and  $u$  is the velocity field. The Pyroelectricity multiphysics interface can then be used to calculate the current density resulting from the temperature change  $dT/dt$ , under fixed-end and free-end conditions, according to Eq. 3

$$J = \frac{dP}{dt} + \frac{d(T(t) - T_0)P^{ET}}{dt} \tag{3}$$

Where  $J$  represents the current flux,  $P$  stands for the material polarization,  $T_0$  is the initial temperature, and  $p^{ET}$  is the total pyroelectric coefficient. Specifically,  $p^{ET}$  is defined as  $p^{ET} = p^{ES} + eE_s\alpha$ , where  $p^{ES}$  denotes the primary pyroelectric coefficient measured at constant strain. The second term in the equation is generally called the secondary coefficient, with piezoelectric coupling matrix  $eES$  and coefficient of thermal expansion  $\alpha$ . The Electrostatics (es) and Electrical Circuit (cir) modules establish fundamental electrical laws and output signals. The Solid Mechanics (solid) and Thermal Expansion (te) modules are used to calculate the thermal strain  $s_{th} = \alpha[T(t) - T_0]$  caused by the temperature change, as well as the corresponding thermal stress  $\sigma_{th} = cE\epsilon_{th}$ , where  $cE$  is the stiffness tensor of the material. Then, Piezoelectric Effect (pze) interface can be implemented to calculate the piezoelectricity-induced polarization based on the linear piezoelectric constitutive equations 4 and 5,

$$S = s_e \sigma + d^T E \tag{4}$$

$$D = d \sigma + \epsilon_T E \tag{5}$$

This equation expresses the relation between strain  $S$ , stress  $\sigma$ , electric field  $E$ , and electric displacement field  $D$ , where  $sE$  represents the elastic compliance tensor under constant electric field, defined as  $s_E = c_E^{-1}$ ,  $d$  is the piezoelectric constant tensor, and  $\varepsilon_p$  denotes the dielectric constant tensor.

The primary pyroelectricity is related to the material's intrinsic property, quantified with the primary pyroelectric coefficient, which has a negative value since electric displacement decreases at higher temperatures when dipoles become more isotropic. Therefore, the primary contribution of pyroelectricity in all four cases (polydomain versus monodomain, ends fixed or not) should be the same, which is  $0.32 \text{ nA/cm}^2$  from the calculation. Therefore, we focus on the differences in secondary pyroelectricity, which is piezoelectricity in essence, and whether the secondary effect works synergistically or counteracts with the primary effect when the film is subjected to different boundary conditions. First, we investigate the monodomain  $CrEl/PbZrT$  NC. When the external electric field  $E$  is neglected, the strain-charge form of pyroelectricity can be defined by Eq. 6.

$$\bar{D} = d\bar{\sigma} = \begin{bmatrix} 0 & 0 & 0 & d_{15} & 0 \\ 0 & 0 & 0 & d_{15} & 0 \\ d_{31} & d_{31} & d_{33} & 0 & 0 \end{bmatrix} \begin{bmatrix} \bar{\sigma}_{11} \\ \bar{\sigma}_{22} \\ \bar{\sigma}_{33} \\ \bar{\sigma}_{23} \\ \bar{\sigma}_{13} \\ \bar{\sigma}_{12} \end{bmatrix} \quad (6)$$

where  $\bar{D}$  is the average electric displacement,  $d$  is the piezoelectric coefficient, and  $\bar{\sigma}$  is the average stress. While a soft matrix embedded with stiff inclusions has a complex stress state at the microscale because of the interfacial contributions and phase mismatches, the primary interest in pyroelectric applications is the overall electrical output (e.g., current and  $\bar{D}$ ). Consequently, we use the average stress  $\bar{\sigma}$  of the entire composite structure in this estimation approach without modeling the intricate local stress field  $\sigma(x, t)$ . Since the output current in the  $z$  direction is measured, the third component of the average electric displacement,  $\bar{D}_3$ , can be described by Eq. 7.

$$\bar{D}_3 = d_{31}\bar{\sigma}_{11} + d_{31}\bar{\sigma}_{22} + d_{33}\bar{\sigma}_{33} \quad (7)$$

Plugging in the parameters for  $PbZrT$  NC, it was obtained Eq. 8

$$\bar{D}_3 = -2.74\bar{\sigma}_{11} - 2.74\bar{\sigma}_{22} + 5.93\bar{\sigma}_{33} \left( \times 10^{-10} C/N \right) \quad (8)$$

For a monodomain  $CrEl/PbZrT$  NC fixed at two ends in the  $x$  direction (Figure 4a), the local stresses in the  $y$  and  $z$  directions tend to cancel out since the film can freely deform in these directions. Therefore, compared to  $\bar{\sigma}_{13}$ , the average stresses  $\bar{\sigma}_{24}$  and  $\bar{\sigma}_{34}$  are approximately zero. Thus, it can estimate the secondary pyroelectric coefficient by Eqs. 8 and 9.

$$\bar{D}_3 \approx -2.74\bar{\sigma}_{11} \left( \times 10^{-10} C/N \right) \quad (8)$$

$$p_2 = \frac{\partial \bar{D}_3}{\partial T} = -2.74 \frac{\partial \bar{\sigma}_{11}}{\partial T} \left( \times 10^{-10} C/N \right) \quad (9)$$

When the  $CrEl/PbZrT$  NC is heated with a positive value of  $\partial \sigma / \partial T$ , a negative secondary pyroelectric coefficient will enhance the output current. Now, we conclude that the output current density is higher than the primary contribution,  $0.32 \text{ nA/cm}^2$ . Theoretical calculations give the estimated output current density of  $\sim 0.50 \text{ nA/cm}^2$  (with fixed ends), which matches with experimental results of  $0.54 \text{ nA/cm}^2$ . The slightly higher value from experiments may come from the nonuniform stress distributions at the microscale.

This approach can be extended to other boundary conditions, for example, a monodomain  $CrEl/PbZrT$  NC with all ends free). Theoretically, the average stresses from all directions are close to zero, although experimentally, it is difficult to meet this. Given that  $\bar{D}_4 \approx 0$  and  $p_2 \approx 0$ , the output current density should be close to the pure primary contribution,  $0.30 \text{ nA/cm}^2$ , which matches with the experimental result,  $0.29 \text{ nA/cm}^2$ .

The discussion on the monodomain  $CrEl/PbZrT$  NC can be partly applied to the polydomain  $CrEl/PbZrT$  featured by the interactions between the  $CrEl$  and  $PbZrT$  NC. In a polydomain phase, since each LC domain is oriented randomly against each other, the overall interactions are canceled out, resulting in little overall secondary pyroelectricity. Therefore, the output current density for the polydomain  $CrEl/PbZrT$  NC should be around  $0.33 \text{ nA/cm}^2$ , which is purely the contribution from the primary pyroelectricity, regardless of whether the film is fixed or not. The current density obtained from experiments ( $0.36$  to  $0.38 \text{ nA/cm}^2$ ) is slightly higher than the calculation, which may be attributed to residual orders in the polydomain film.

The secondary contribution to pyroelectricity is dependent on  $CrEl$  alignment and the boundary conditions. The monodomain  $CrEl/PbZrT$  under fixed boundary conditions shows the highest secondary effect that enhances the overall pyroelectricity. The polydomain  $CrEl/PbZrT$  shows weak secondary effects according to experiments. Nonfixed monodomain  $CrEl/PbZrT$  has reduced overall pyroelectricity. We note that all the discussions above are based on the composite films with  $30.1 \text{ wt } \% PbZrT$  loading, and the highest possible  $PbZrT$  loading is  $44.7 \text{ wt } \%$  instead of  $60.1 \text{ wt } \%$  for the monodomain  $CrEl/PbZrT$  NC since the samples at higher  $PbZrT$  loadings crack when stretched. Under fixed boundary conditions, the monodomain  $CrEl/PbZrT$  NC ( $44.7 \text{ wt } \% PbZrT$ ) shows a peak output current of  $2.81 \text{ nA}$  and a voltage of  $6.23 \text{ V}$ , yielding a pyroelectric coefficient of  $-4.09 \text{ nC cm}^{-2} \text{ K}^{-1}$ , whose magnitude is  $52\%$  higher than that of the widely used flexible pyroelectric polymer PVDF ( $-2.40 \text{ nC cm}^{-2} \text{ K}^{-1}$ ) (13).

### The effect of $CrEl$ NC mechanical properties on the pyroelectric performance of $CrEl/PbZrT$ NCs

Whether the mechanical property of the  $CrEl$  NC affects the pyroelectric performance depends on the  $CrEl$  disturbances. For polydomain  $CrEl/PbZrT$  NC, the mechanical property of the  $CrEl$  NC has no a significant influence on the pyroelectric performance. That is because they have little secondary

**Table 2:** The mechanical performance and pyroelectric current density of the monodomain LCE/PZT.

Content	Results
PET MP (g)	0,269
EDDT (g)	1,41
Yang 's modulus (MPa)	1,70

pyroelectricity due to the little thermal stress generated in polydomain *CrEI*. Therefore, the pyroelectric output of polydomain *CrEI/PbZrT NC* all comes from the primary pyroelectricity, which only relies on the mass loading of *PbZrT NC*. Similarly, for monodomain *CrEI/PbZrT NC* with free boundary conditions, the secondary pyroelectricity is nearly zero due to the negligible average stress. For monodomain *CrEI/PbZrT NC* with the two longitudinal ends fixed, the mechanical property of the *CrEI NC* can affect the pyroelectric performance, since the secondary pyroelectricity makes a difference now. A higher Young's modulus can give a higher thermal stress, thus enhancing the secondary pyroelectricity. A higher thermal expansion coefficient gives a larger thermal strain, which leads to enhanced thermal stress and secondary pyroelectricity. However, in real cases, the Young's modulus and thermal expansion coefficient change simultaneously, making it difficult to decouple their separate effect. Therefore, to test the effect of *CrEI NC* mechanical properties on the pyroelectric performance in real situations, we fabricated monodomain *CrEI/PbZrT NC* with a *PbZrT* ratio of 31.1 wt% with different molar ratios of PETMP. It was measured their Young's moduli and their thermal expansion coefficients. It was measured their pyroelectric currents, and conducted FEM simulations using the measured parameters as new input to verify the experiments. The results are summarized in Table 2. When the molar ratio of EDDT to PETMP was low (e.g., 9.6 in, the relatively high amount of crosslinker PETMP would make the polymer brittle, which fractured during the two-step crosslinking process. When the molar ratio of acrylates to thiols was too high, the degree of polymerization was too low to form a film after the Michael addition reaction, thus the two-step crosslinking could not proceed. It was detected that monodomain films were produced successfully. When the molar ratio of EDDT to PETMP was the highest, the lowest Young's modulus was obtained as 0.66 MPa, and reduced secondary pyroelectricity was observed. Meanwhile, a lower Young's modulus led to a higher absolute value of thermal expansion coefficient, which enhanced the secondary pyroelectricity. Therefore, Young's modulus and thermal expansion coefficient counteract with each other regarding the secondary pyroelectricity. This proves again that they cannot be decoupled. For the pyroelectric current density, give the highest experimental results of 0.59 nA/cm<sup>2</sup>. It was observed that the highest current density was obtained. Therefore, we can conclude that the effect of the Young's modulus dominates. When the Young's modulus was either too high or too low the fabrication of the the monodomain films were not performed.

## Conclusion

The generation of *CrEI/PbZrT* pyroelectric energy harvester significantly enhanced pyroelectricity because of the secondary

pyroelectricity generated from *CrEI* thermal stress. The effect of secondary pyroelectricity on the overall pyroelectric output is dependent on *CrEI* boundary conditions. The monodomain *CrEI/PbZrT* under fixed boundary conditions exhibits the highest secondary pyroelectric effect, with the output current density increased from 0.38 nA/cm<sup>2</sup> to 0.64 nA/cm<sup>2</sup>.

The fixed monodomain *CrEI/PbZrT NC* film with a *PbZrT* ratio of 49.9 wt % exhibited an output current of 3.22 nA and a voltage of 6.89 V at a maximum heating rate of 0.25 K s<sup>-1</sup>, which is 54% higher than that of the widely used flexible pyroelectric polymer PVDF. The *CrEI/PbZrT NCs* can be used as a power source to harvests the heat to drive flexible electronics such as LEDs, digital watches, and sensors.

Liquid crystalline elastomer (*CrEI*) and pyroelectric lead zirconate titanate (*PbZrT*) nanoparticles demonstrate a flexible heat harvesting device with high output. The overall pyroelectricity is enhanced by the secondary pyroelectricity generated from the thermal stress imposed on the *CrEI*.

## References

- Mahapatra SD, Mohapatra PC, Aria AI, Christie G, Mishra YK, Hofmann S, et al. Piezoelectric materials for energy harvesting and sensing applications: roadmap for future smart materials. *Adv Sci (Weinh)*. 2021;8(17):e2100864. Available from: <https://doi.org/10.1002/advs.202100864>
- Sukumaran S, Chatbouri S, Rouxel D, Tisserand E, Thiebaud F, Ben Zineb T. Recent advances in flexible PVDF based piezoelectric polymer devices for energy harvesting applications. *J Intell Mater Syst Struct*. 2021;32:746-780. Available from: <https://doi.org/10.1177/1045389X20966058>
- Khan MSA, Hoq MT, Karim AHMZ, Alam MK, Howlader M, Rajkumar RK. Energy harvesting-technical analysis of evolution, control strategies, and future aspects. *J Electron Sci Technol*. 2019;17:116-125. Available from: <https://doi.org/10.11989/JEST.1674-862X.80314201>
- Sahu M, Hajra S, Lee K, Deepti P, Mistewicz K, Kim HJ. Piezoelectric nanogenerator based on lead-free flexible PVDF-barium titanate composite films for driving low power electronics. *Crystals*. 2021;11:1-10. Available from: <https://doi.org/10.3390/cryst11020085>
- Ghosh SK, Mandal D. Synergistically enhanced piezoelectric output in highly aligned 1D polymer nanofibers integrated all-fiber nanogenerator for wearable nano-tactile sensor. *Nano Energy*. 2018;53:245-257. Available from: <https://doi.org/10.1016/j.nanoen.2018.08.036>
- Mistewicz K. Pyroelectric nanogenerator based on an SbS<sub>1</sub>-TiO<sub>2</sub> nanocomposite. *Sensors (Basel)*. 2021;22(1):69. Available from: <https://doi.org/10.3390/s22010069>
- Bowen CR, Taylor J, Leboubar E, Zabeck D, Chauhan A, Vaish R. Pyroelectric materials and devices for energy harvesting applications. *Energy Environ Sci*. 2014;7:3836-3856. Available from: <https://pubs.rsc.org/en/content/articlelanding/2014/ee/c4ee01759e>
- Lang SB, Das-Gupta DK. Chapter 1 – Pyroelectricity: Fundamentals and Applications. 2001. Available from: <https://doi.org/10.1016/B978-012513745-4/50036-6>
- Lang SB. Pyroelectricity: from ancient curiosity to modern imaging tool. *Phys Today*. 2005;58:31-36. Available from: <https://ui.adsabs.harvard.edu/abs/2005PhT....58h..31L>
- Korkmaz S, Kariper A. Pyroelectric nanogenerators (PyNGs) in converting thermal energy into electrical energy: fundamentals and current status. *Nano Energy*. 2021;84:105888. Available from: <https://doi.org/10.1016/j.nanoen.2021.105888>
- Thakre A, Kumar A, Song HC, Jeong DY, Ryu J. Pyroelectric energy conversion and its applications—flexible energy harvesters. *Sensors (Basel)*. 2019;19:1-25. Available from: <https://doi.org/10.3390/s19092170>



12. Xue H, Yang Q, Wang D, Luo W, Wang W, Lin M, et al. A wearable pyroelectric nanogenerator and self-powered breathing sensor. *Nano Energy*. 2017;38:147-154. Available from: <https://doi.org/10.1016/j.nanoen.2017.05.056>
13. Yang Y, Zhang H, Zhu G, Lee S, Lin ZH, Wang ZL. Flexible hybrid energy cell for simultaneously harvesting thermal, mechanical, and solar energies. *ACS Nano*. 2013;7:785-790. Available from: <https://doi.org/10.1021/nn305247x>
14. Yang Y, Wang S, Zhang Y, Wang ZL. Pyroelectric nanogenerators for driving wireless sensors. *Nano Lett*. 2012;12(12):6408-6413. Available from: <https://doi.org/10.1021/nl303755m>
15. Clementi G, Margueron S, Suarez MA, Baron T, Dulmet B, Bartaszyte A. Piezoelectric and pyroelectric energy harvesting from lithium niobate films. *J Phys Conf Ser*. 2019;1407:012039. Available from: <https://iopscience.iop.org/article/10.1088/1742-6596/1407/1/012039>
16. Yang Y, Jung JH, Yun BK, Zhang F, Pradel KC, Guo W, et al. Flexible pyroelectric nanogenerators using a composite structure of lead-free KNbO<sub>3</sub> nanowires. *Adv Mater*. 2012;24:5357-5362. Available from: <https://doi.org/10.1002/adma.201201414>
17. Wu CM, Chou MH, Chala TF, Shimamura Y, Murakami R. Infrared-driven poly(vinylidene difluoride)/tungsten oxide pyroelectric generator for non-contact energy harvesting. *Compos Sci Technol*. 2019;178:26-32. Available from: <https://doi.org/10.1016/j.compscitech.2019.05.004>
18. Zabek D, Taylor J, Le Boulbar E, Bowen CR. Micropatterning of flexible and free standing polyvinylidene difluoride (PVDF) films for enhanced pyroelectric energy transformation. *Adv Energy Mater*. 2015;5:1-6. Available from: <https://doi.org/10.1002/aenm.201401891>
19. He H, Lu X, Hanc E, Chen C, Zhang H, Lu L. Advances in lead-free pyroelectric materials: a comprehensive review. *J Mater Chem C*. 2020;8:1494-1516. Available from: <https://pubs.rsc.org/en/content/articlelanding/2020/tc/c9tc05222d>
20. Lee JH, Lee KY, Gupta MK, Kim TY, Lee DY, Oh J, et al. Highly stretchable piezoelectric-pyroelectric hybrid nanogenerator. *Adv Mater*. 2014;26:765-769. Available from: <https://doi.org/10.1002/adma.201303570>
21. Ruan L, Yao X, Chang Y, Zhou L, Qin G, Zhang X. Properties and applications of the  $\beta$  phase poly(vinylidene fluoride). *Polymers (Basel)*. 2018;10. Available from: <https://doi.org/10.3390/polym10030228>
22. Li Q, Zhao J, He B, Hu Z. Solution processable poly(vinylidene fluoride)-based ferroelectric polymers for flexible electronics. *APL Mater*. 2021;9. Available from: <https://doi.org/10.1063/5.0035539>
23. Krishnamoorthy K, Mariappan VK, Pazhamalai P, Sahoo S, Kim SJ. Mechanical energy harvesting properties of free-standing carbyne enriched carbon film derived from dehydrohalogenation of polyvinylidene fluoride. *Nano Energy*. 2019;59:453-463. Available from: <https://doi.org/10.1016/j.nanoen.2019.02.041>
24. Pazhamalai P, Krishnamoorthy K, Mariappan VK, Sahoo S, Manoharan S, Kim SJ. A high efficacy self-charging MoSe<sub>2</sub> solid-state supercapacitor using electrospun nanofibrous piezoelectric separator with ionogel electrolyte. *Adv Mater Interfaces*. 2018;5:1800055. Available from: <https://doi.org/10.1002/admi.201800055>
25. Mariappan VK, Krishnamoorthy K, Manoharan S, Pazhamalai P, Kim SJ. Electrospun polymer-derived carbyne supercapacitor for alternating current line filtering. *Small*. 2021;17:2102971. Available from: <https://doi.org/10.1002/smll.202102971>
26. Saxena P, Shukla P. A comprehensive review on fundamental properties and applications of poly(vinylidene fluoride) (PVDF). *Adv Compos Hybrid Mater*. 2021;4:8-26. Available from: <https://link.springer.com/article/10.1007/s42114-021-00217-0>
27. Low YKA, Meenuharathi N, Niphadkar ND, Boey FYC, Ng K.  $\alpha$ - and  $\beta$ -poly(vinylidene fluoride) evoke different cellular behaviours. *J Biomater Sci Polym Ed*. 2012;23:1651-1667. Available from: <https://doi.org/10.1163/092050610X519471>
28. Gusarov B, Gusarova E, Viala B, Gimeno L, Boisseau S, Cugat O, et al. Thermal energy harvesting by piezoelectric PVDF polymer coupled with shape memory alloy. *Sens Actuators A Phys*. 2016;243:175-181. Available from: <https://doi.org/10.1016/j.sna.2016.03.026>
29. Panwar LS, Panwar V, Anoop G, Park S. Carbon nanofiber-polyelectrolyte triggered piezoelectric polymer-based hydrophilic nanocomposite for high sensing voltage generation. *J Mater Res Technol*. 2022;17:3246-3261. Available from: <https://doi.org/10.1016/j.jmrt.2022.02.075>
30. Cai X, Lei T, Sun D, Lin L. A critical analysis of the  $\alpha$ ,  $\beta$  and  $\gamma$  phases in poly(vinylidene fluoride) using FTIR. *RSC Adv*. 2017;7:15382-15389. Available from: <https://pubs.rsc.org/en/content/articlelanding/2017/ra/c7ra01267e>
31. Nishiyama T, Sumihara T, Sasaki Y, Sato E, Yamato M, Horibe H. Crystalline structure control of poly(vinylidene fluoride) films with the antisolvent addition method. *Polym J*. 2016;48:1035-1038. Available from: <https://www.nature.com/articles/pj201662>
32. Panwar V, Kang B, Park J, Park S, Mehra RM. Study of dielectric properties of styrene-acrylonitrile graphite sheets composites in low and high frequency region. *Eur Polym J*. 2009;45:1777-1784. Available from: <https://doi.org/10.1016/j.eurpolymj.2009.02.020>
33. Almond DP, Bowen CR. An explanation of the photoinduced giant dielectric constant of lead halide perovskite solar cells. *J Phys Chem Lett*. 2015;6:1736-1740. Available from: <https://doi.org/10.1021/acs.jpcclett.5b00620>
34. Panwar V, Gill FS, Rathi V, Tewari VK, Mehra RM, Park JO, et al. Fabrication of conducting composite sheets using cost-effective graphite flakes and amorphous styrene acrylonitrile for enhanced thermistor, dielectric, and electromagnetic interference shielding properties. *Mater Chem Phys*. 2017;193:329-338. Available from: <https://doi.org/10.1016/j.matchemphys.2017.02.050>
35. Jayakumar OD, Abdelhamid EH, Kotari V, Mandal BP, Rao R, Jagannath, Naik VM, et al. Fabrication of flexible and self-standing inorganic-organic three phase magneto-dielectric PVDF based multiferroic nanocomposite films through a small loading of graphene oxide (GO) and Fe<sub>3</sub>O<sub>4</sub> nanoparticles. *Dalton Trans*. 2015;44:15872-15881. Available from: <https://doi.org/10.1039/c5dt01509j>
36. Dash S, Choudhary RNP, Kumar A, Goswami MN. Enhanced dielectric properties and theoretical modeling of PVDF-ceramic composites. *J Mater Sci Mater Electron*. 2019;30:19309-19318. Available from: <https://link.springer.com/article/10.1007/s10854-019-02291-z>
37. Gupta S, Bhunia R, Fatma B, Maurya D, Singh D, Gupta R, et al. Multifunctional and flexible polymeric nanocomposite films with improved ferroelectric and piezoelectric properties for energy generation devices. *ACS Appl Energy Mater*. 2019;2:6364-6374. Available from: <https://pure.psu.edu/en/publications/multifunctional-and-flexible-polymeric-nanocomposite-films-with-i>

## Discover a bigger Impact and Visibility of your article publication with Peertechz Publications

### Highlights

- ❖ Signatory publisher of ORCID
- ❖ Signatory Publisher of DORA (San Francisco Declaration on Research Assessment)
- ❖ Articles archived in worlds' renowned service providers such as Portico, CNKI, AGRIS, TDNet, Base (Bielefeld University Library), CrossRef, Scilit, J-Gate etc.
- ❖ Journals indexed in ICMJE, SHERPA/ROME0, Google Scholar etc.
- ❖ OAI-PMH (Open Archives Initiative Protocol for Metadata Harvesting)
- ❖ Dedicated Editorial Board for every journal
- ❖ Accurate and rapid peer-review process
- ❖ Increased citations of published articles through promotions
- ❖ Reduced timeline for article publication

Submit your articles and experience a new surge in publication services

<https://www.peertechzpublications.org/submission>

Peertechz journals wishes everlasting success in your every endeavours.